ACS Partner Journal

ACCOUNTS
—of materials research—

pubs.acs.org/amrcda

Article

An Account of Chiral Metal Surfaces and Their Enantiospecific Chemistry

Andrew J. Gellman*

Cite This: *Acc. Mater. Res.* 2021, 2, 1024–1032

Read Online

ACCESS | Metrics & More | Article Recommendations

CONSPECTUS: Molecular chirality has been of scientific interest since 1848 when Pasteur demonstrated its direct connection to the rotation of light by solutions of chiral compounds. In the 1960s the connection was made between the chirality of pharmaceutical compounds and their physiological impact; one enantiomer can be therapeutic while the other is toxic. That realization prompted enormous effort in the synthesis of enantiomerically pure compounds for bioactive use (a $300B/yr market). Until relatively recently, metals were ignored as potential substrates for asymmetric surface chemistry because metals have highly symmetric, *achiral* bulk structures and the premise was that they could not expose chiral surfaces. In 1996, we demonstrated that the high Miller index surfaces of metals can be chiral, existing in two enantiomeric forms $M(hkl)^{R\&S}$, and we hypothesized that they exhibit enantiospecific interactions with chiral adsorbates. Most such intrinsically chiral metal surfaces have ideal structural motifs based on low Miller index terraces separated by kinked monatomic steps. This Account begins with a short tutorial on the ideal and real structures of chiral metal surfaces to provide a firm basis for understanding the origin of their chirality. It then chronicles the evolution of our understanding of their enantiospecific interactions with chiral adsorbates.

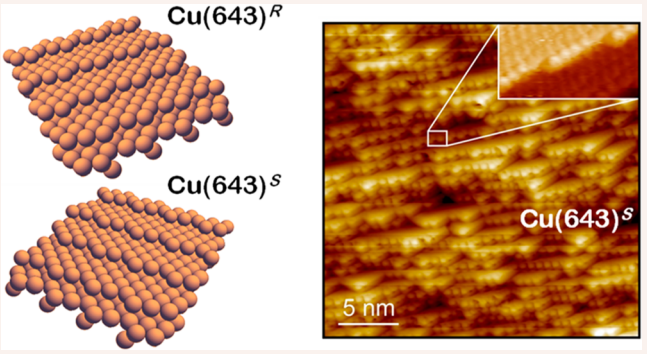

Detecting, quantifying, and understanding enantiospecific surface chemistry on intrinsically chiral metal surfaces has been far more challenging than coming to the realization that such surfaces exist. The first successes came from measurements and modeling of the enantiospecific adsorption energetics of small chiral molecules such as propylene oxide and *trans*-1,2-dimethylcyclopropane. These revealed one of the core challenges to observing enantiospecificity, the fact that the enantiospecificities of reaction energetics and barriers tend to be small, i.e., a few kJ/mol. Measurements of the enantiospecific adsorption energetics of *R*-3-methylcyclohexanone on seven different $Cu(hkl)^{R\&S}$ surfaces demonstrated their sensitivity to surface structure, but again revealed variations of only a few kJ/mol. One of the most important advances in our understanding of chiral surface chemistry is that the limitations imposed by weakly enantiospecific interactions can be circumvented by processes with nonlinear kinetics or equilibria. As an example, the surface explosion mechanism of D- and L-tartaric acid decomposition on $Cu(hkl)^{R\&S}$ surfaces leads to enantiospecific rates that differ by almost 2 orders of magnitude, in spite of the fact that the rate constants are only weakly enantiospecific. More surprising is the observation that equilibrium adsorption of nonracemic mixtures of D- and L-aspartic acid can lead to autoamplification of enantiomeric excess, even on achiral Cu(111) surfaces. Again, this arises from a nonlinear adsorption isotherm. Most recently, we have developed a high throughput method for identification of the most enantiospecific surface orientation for a given reaction from the continuum of $Cu(hkl)^{R\&S}$ surface orientations. These developments, and others described in this Account, firmly establish some of the basic principles of chiral surface chemistry.

1. INTRODUCTION – CHIRALITY

Chiral objects are nonsuperimposable on their mirror images and exist in left- and right-handed forms known as enantiomers. This seemingly simple geometric property leads to intriguing and important physical and chemical properties of chiral molecules, materials, and surfaces. The surfaces of chiral crystalline materials must also be chiral. Less obvious is the fact that the surfaces of achiral crystalline materials can also be intrinsically chiral. Twenty-five years ago, we demonstrated that single crystalline metal surfaces can be chiral (Figure 1).[1] The

Received: June 28, 2021
Revised: September 14, 2021
Published: October 28, 2021

https://doi.org/10.1021/accountsmr.1c00145
Acc. Mater. Res. 2021, 2, 1024–1032

intervening period has developed our current understanding of the enantiospecific physical and chemical properties of intrinsically chiral metal surfaces.[2,3]

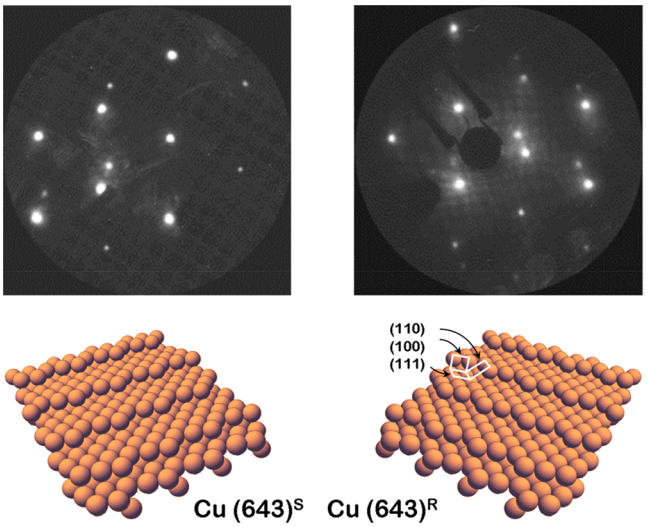

Figure 1. Intrinsically chiral metal surfaces. Ideal atomic structures of the chiral $Cu(643)^{R\&S}$ surfaces. The kinked step edges break mirror symmetry, rendering the two structures enantiomorphous. Close inspection reveals that the terraces are nanofacets of the hexagonal close-packed (111) plane, the straight step edges are nanofacets of the square (100) plane, and the kinks are nanofacets of the rectangular (110) plane. The low energy electron diffraction patterns from these two surfaces are also enantiomorphous. The split spots are oriented toward one o'clock for $Cu(643)^S$ and toward 11 o'clock for $Cu(643)^R$ demonstrating that the surface structures are chiral enantiomers of one another. Reproduced with permission from ref 14. Copyright 2001 Elsevier.

All of the complex biomolecules such as DNA, sugars, and amino acids that serve as the basis for life on Earth are chiral but only occur in single enantiomer form in nature.[4−6] One consequence of biomolecular enantiopurity is that synthetic chiral pharmaceuticals must be manufactured and administered in enantiomerically pure form. This enantioselective synthesis is arguably one of the most challenging forms of chemical processing.[7] The widespread use of surfaces for chemical processing suggests that chiral surfaces could be used to achieve enantioselectivity in processes such as catalysis, adsorption, and crystal nucleation.

2. INTRINSICALLY CHIRAL METAL SURFACES

Switzer et al. have published a useful table summarizing those crystal systems and lattice plane orientations (Miller indices) that expose chiral surfaces.[8] Pure metals have achiral bulk structures; however, they expose chiral surfaces when the surface normal does not lie in any of the bulk crystal mirror planes. This holds for the surface orientations, (hkl), with $h \times k \times l \neq 0$ and $h \neq k \neq l \neq h$.[9] It is important to note that some metallic alloys and inorganic compounds such as PdGa, Te, and HgS have chiral bulk crystal structures and, therefore, expose chiral surfaces, even for their high symmetry, low Miller index surface orientations.[10−13] These materials can also exhibit enantiospecific surface chemistry.

This Account focuses on the intrinsically chiral surfaces of pure metals and on their enantiospecific surface properties and surface chemistry. The first suggestion that a pure metal single crystal surface could be chiral was published ∼25 years ago.[1,2] That work used low energy electron diffraction (LEED) from the Ag(643) and Ag $(\overline{643})$ surfaces to demonstrate their enantiomorphous relationship to one another. Figure 1 shows equivalent LEED patterns for the Cu(643) and Cu $(\overline{643})$ surfaces and illustrations of their ideal atomic structures.[14] These are high Miller index surfaces with structures formed by (111) terraces separated by kinked step edges consisting of (100) step nanofacets separated by single atom (110) kinks. The clockwise rotational order of progression from (111) → (100) → (110) is used to label one surface enantiomer $Cu(643)^R$ while $Cu(643)^S$ exhibits counterclockwise rotation from (111) → (100) → (110). The enantiomorphous relationship of the two structures should be clear. The LEED patterns in Figure 1 can be described roughly as a set of spots forming a hexagonal pattern. The spots are each split into pairs by the presence of the step edges with the LEED pattern from the $Cu(643)^S$ surface exhibiting splitting toward one o'clock while the LEED from the $Cu(643)^R$ surface exhibits splitting toward 11 o'clock. The enantiomorphous relationship between the two LEED patterns reflects the enantiomorphous relationship between the chiral surfaces.

The history of intrinsically chiral metal surfaces begins in 1996 with the demonstration of the chirality of $Ag(643)^R$ and $Ag(643)^S$ via their LEED patterns.[1,2] The first demonstration of enantiospecific interactions between chiral adsorbates and intrinsically chiral metal surfaces was performed by Sholl in 1998 using Monte Carlo simulations to estimate the enantiospecificities of the adsorption energies and orientations of small chiral alkanes such as *trans*-1,2-dimethylcyclopropane on various chiral $Pt(hkl)^{R\&S}$ surfaces.[15] The first experimental demonstration of enantiospecific surface chemistry was made by Attard et al. in 1999 using electrochemical methods to demonstrate a diastereomeric relationship in the electrooxidation kinetics of D- and L-glucose on chiral $Pt(643)^{R\&S}$ electrodes.[16] The first experimental corroboration of enantiospecific chemistry on intrinsically chiral metal surfaces was reported by us in 2001. Careful measurements of the thermal desorption kinetics of *R*- and *S*-propylene oxide (PO) and *R*-3-methylcyclohexanone (*R*-3MCHO) from chiral $Cu(643)^{R\&S}$ surfaces revealed enantiospecific desorption energies.[14,17]

3. STRUCTURE OF INTRINSICALLY CHIRAL METAL SURFACES

3.1. Ideal Chiral Surface Structures

The ideal structure of a chiral surface is predicted by cleaving the bulk crystal along a low symmetry plane and assuming that the atoms on either side of the plane rigidly retain their positions relative to the bulk lattice (Figure 1). As mentioned earlier, these surfaces can be thought to have structures based on the intersection of the three high symmetry, low Miller index planes projecting out of the bulk to form terrace, step, and kink nanofacets.[18] For a given chiral surface orientation, the motif describing the surface structure can characterized by first identifying which of the six combinations of the low Miller index nanofacets form the terrace, step, and kink. At the second level, intrinsically chiral surfaces are distinguished by the spacing between the steps and by the spacing between the kinks along the straight step edges.

The set of all possible intrinsically chiral metal surfaces forms a 2D continuum that is best understood by considering a spherical face-centered-cubic nanoparticle (Figure 2). The low

https://doi.org/10.1021/accountsmr.1c00145
Acc. Mater. Res. 2021, 2, 1024−1032

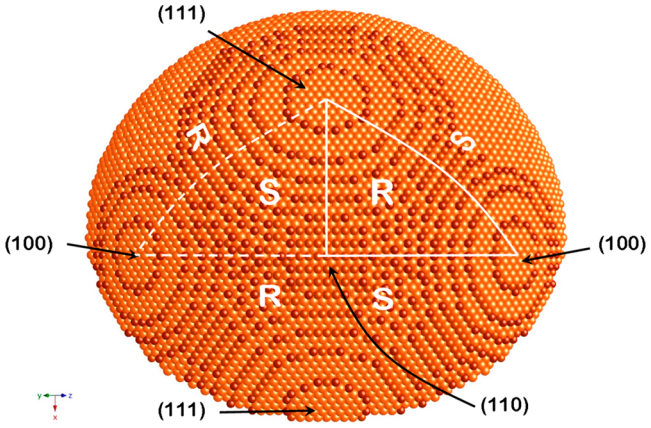

Figure 2. Stereographic triangle of surface orientations. Illustration of a ∼5 nm diameter spherical nanocrystal with a face-centered-cubic bulk structure. The sphere exposes bulk crystal planes oriented tangentially to the surface of the sphere and perpendicular to the surface normal at any point. The low Miller index planes lie perpendicular to the high symmetry directions of the FCC lattice. They expose achiral nanofacets with mirror symmetry. These define the vertices of the stereographic triangle. Surfaces exposed at the points along the edges of the stereographic triangle also have mirror symmetry and are achiral. All surfaces exposed at points interior to the stereographic triangle lack any mirror symmetry and are chiral. By convention, all surfaces within one triangle have the same chirality. Surfaces exposed by edge sharing triangles are of opposite chirality.

Miller index directions can be seen by the projections of the (111), (110), and (100) facets. These facets define a set of 48 nominally equivalent triangles spanning the nanoparticle surface. The diagram in Figure 2 effectively illustrates the projection of two such stereographic triangles onto the (110) plane. Every point in or on such a stereographic triangle is uniquely mapped onto one of the continuous distribution of possible surface orientations. All surface orientations falling outside the triangle can be mapped onto surfaces within the triangle by symmetry operations of the bulk lattice. The three low Miller index surfaces have multiple bulk lattice mirror planes projecting normal to the surfaces and are, therefore, achiral. The surfaces denoted by points on the edges of the stereographic triangle also have a bulk mirror plane oriented perpendicular to the surface and are, therefore, achiral. The points interior to the triangle represent surface orientations with no mirror symmetry and these are, therefore, chiral. This framework for considering surface chirality reveals the fact that that there are infinitely many more chiral surface orientations than achiral surface orientations.

The last point to make regarding the ideal structures of intrinsically chiral metal surfaces addresses the conventions used for assigning the handedness; there are several.[1,2,16,19,20] In this Account we have used the convention based on the sense of rotation of the low Miller index directions around the surface normal; *R*- (*S*-) corresponds to a clockwise (counterclockwise) progression for [111] → [100] → [110].

3.2. Real Structures of Intrinsically Chiral Surfaces

The ideal structures of surfaces discussed in the previous section do not represent reality. It is well understood in the field of surface science that the positions of atoms at the surfaces of real metals can deviate substantially from ideality. One form of reconstruction that has been observed on high Miller index surfaces is known as "step bunching" in which monatomic steps coalesce to form facets that can be two or more atoms high.[21,22] Such reconstructions on chiral surfaces could, in principle, result in structures with large achiral facets. However, scanning tunneling micrographs of chiral Cu(*hkl*)$^{R\&S}$ surfaces show no evidence of step bunching.[23−25]

Cu(*hkl*)$^{R\&S}$ surfaces are subject to roughening which is driven by entropy gain at high temperatures. This was first recognized and studied by Sholl et al. using kinetic Monte Carlo simulations of the chiral Pt(643)^{S} surface.[9,26] Figure 3A shows an illustration

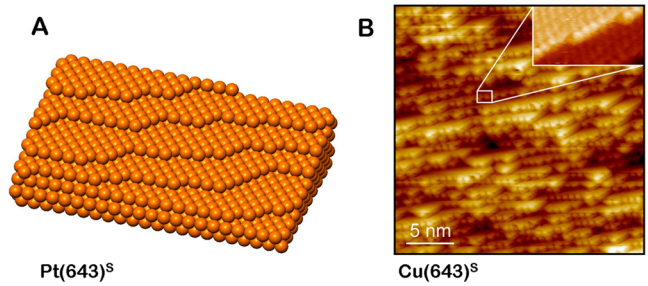

Figure 3. Thermally roughened chiral surfaces. The real structures of surfaces differ from their ideal structure predicted by the bulk lattice structure. A) The structure of Pt(643)^{S} predicted by Monte Carlo simulation at 500 K reveals the consequences of thermal roughening. The ideal structure (Figure 1) has evolved by diffusion of atoms along the steps edge, leading to the coalescence of kinks and the formation of long runs of close-packed (100) and (110) step edges. The areal density of kinks is reduced but they retain their original chirality. B) Atomic resolution STM image of the Cu(643)^{S} at 78 K reveals evenly spaced step edges with roughened structure very similar to that predicted by simulation. Reproduced with permission from ref 25. Copyright 2008 American Chemical Society.

of the Pt(643)^{S} surface after simulated annealing at 500 K. The roughened structure reveals a reduction in the areal kink density as a result of kink coalescence and the formation of kinks at the intersections of long step edges of various lengths. One of the key observations from this work is that there was no observable formation of *R*-kinks. In spite of the thermal roughening, the surface retained its net *S*-chirality.

Thermal roughening on intrinsically chiral surfaces has been borne out by scanning tunneling microscopy of intrinsically chiral Cu(643) (Figure 3B) and Pt(531) surfaces.[25,27] Figure 3B reveals a real Cu(643)^{S} surface structure very similar to that predicted by simulation of thermal roughening for Pt(643)^{S}, i.e., monatomic steps that are kinked but with kinks unevenly distributed along the step edge. The scanning tunneling micrograph reveals that the kink density is reduced by about 25% relative to that of the ideal surface structure. Nonetheless, the key point is that, while thermal roughening does result in a reduction of kink density, the net chirality of the Cu(643)^{S} surface is retained.

4. ENANTIOSPECIFIC ADSORBATE ORIENTATION

A large body of work has studied the structures and long-range order of chiral compounds on achiral low Miller index surfaces.[3,28−31] In those cases, the two enantiomeric structures should be nonsuperimposable mirror images of one another. Enantiomer adsorption on chiral surfaces should result in the formation of diastereomers that are no longer identical but have properties that obey $R/R \equiv S/S \not\equiv R/S \equiv S/R$.[32] Enantiomer orientation reveals such diastereomerism.

https://doi.org/10.1021/accountsmr.1c00145
Acc. Mater. Res. 2021, 2, 1024−1032

4.1. Simulation of Chiral Adsorbate Orientation

Atomistic structure is one of the common outputs of atomistic simulations. The first demonstrations by Sholl of enantiospecific adsorption on intrinsically chiral metal surfaces simulated chiral alkanes on chiral Pt(hkl)$^{R\&S}$ using Monte Carlo methods.[15] For *trans*-1,2-dimethylcyclopropane, the CH_3C-CCH_3 bond orientation relative to the surface was used as a proxy for adsorbate orientation. The probability distributions of the polar angles, (θ, φ), describing the adsorbate orientations on a Pt(643)^S surface revealed clear differences between the orientations of the two molecular enantiomers.

The first use of Density Functional Theory (DFT) on an intrinsically chiral surface studied Pt(531).[27] Since then, DFT has been used to study the adsorption and structure of amino acids and other chiral adsorbates on chiral metal surfaces. A very nice example coupled DFT with X-ray photoelectron spectroscopy and X-ray photoelectron diffraction to reveal the enantiospecific orientation of D- and L-cysteine adsorbed on chiral Au(17,11,9)^S.[33,34] For D-Cys, the deprotonated thiolate group (C−S−Au) binds to the (100) step edge while the amine group ($C-NH_2-Au$) binds to the (110) kink and vice versa for L-Cys. The carboxyl groups ($C-CO_2H$) project out over the (111) terrace in both cases.

4.2. Experimental Observation of Chiral Adsorbate Orientation

A variety of surface analysis tools provide experimental insight into adsorbate structure and orientation on surfaces. These include LEED,[35] infrared reflection absorption spectroscopy (IRAS),[14,36] near edge X-ray absorption fine structure spectroscopy (NEXAFS),[37,38] and X-ray photoelectron diffraction (XPD).[33,34] Applied to chiral adsorbates on intrinsically chiral surfaces these can provide experimental insight into the enantiospecificity of chiral adsorbate orientation.

Infrared absorption is not commonly thought of as a probe of molecular structure, but on metal surfaces the intensities, **I**, of vibrational modes observed in reflection absorption infrared spectroscopy are dictated by the projection of their dynamic dipole vectors, $\vec{\mu}$, onto the surface normal, $\hat{n}$. The intensity is given by $\mathbf{I} \propto |\vec{\mu}|^2 \cdot \cos^2 \theta_{\vec{\mu}\hat{n}}$; i.e., a vibrational mode with its dynamic dipole moment parallel to the surface, $\theta_{\vec{\mu}\hat{n}} = 90°$, will exhibit no intensity, **I**. If the vibrational spectrum of an adsorbate is sufficiently well understood, the mode intensities can be used to estimate quantitatively its orientation relative to the surface normal.[39,40]

In the context of chiral adsorbates on intrinsically chiral metal surfaces, vibrational mode intensities have been used to observe enantiospecificity of adsorbate orientation by comparing vibration mode intensities in reflection infrared absorption spectra obtained from diastereomerically related sets of adsorbate/substrate. The first evidence of enantiospecific adsorbate orientation comes from spectra of *R*- and *S*-2-butanoxy groups on Ag(643)^R.[14] One pair of modes associated with C−H stretch motions and another pair associated with CH_2 scissor and CH_3 deformation motions each exhibit an inversion of intensity between to two adsorbate enantiomers. This signals an enantiospecific difference in the orientations of CH bonds and, hence, the overall molecular orientation on the surface.

The most detailed infrared absorption study of a chiral adsorbate/substrate pair is the case of *R*-3-methylcyclohexanone on Cu(643)$^{R\&S}$.[36] The spectra in Figure 4A show *R*-3MCHO adsorbed at multilayer coverage and monolayer coverage and

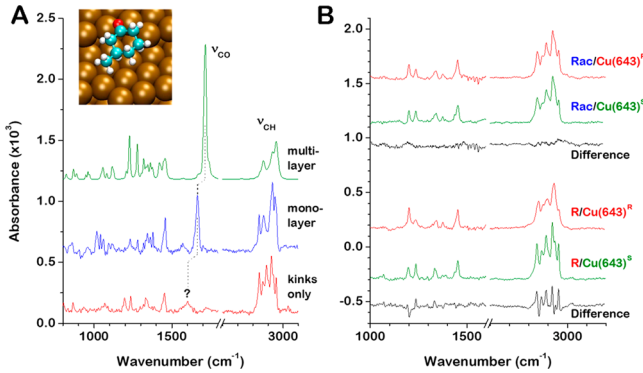

Figure 4. Enantiospecific adsorbate orientation on chiral surfaces. A) FT-IRRAS spectra obtained from *R*-3MCHO on the Cu(643)^R surfaces at multilayer coverage, at monolayer coverage, and after adsorption only at the kink sites. The inset shows the orientation predicted by DFT for *R*-3MCHO adsorbed at the kinks on the Cu(643)^R surfaces. The lowering of the $\nu_{C=O}$ stretch frequency indicates that the ketone group is contributing significantly to the interaction with the surface. The substantial decrease in its intensity relative to the ν_{CH} modes suggests that, when *R*-3MCHO is adsorbed at the kinks, the C=O bond lies roughly parallel to the surface, as illustrated in the inset. B) FT-IRAS spectra of racemic 3MCHO and of *R*-3MCHO adsorbed at the kinks on the Cu(643)$^{R\&S}$ surfaces. The control experiment using the racemic 3MCHO reveals that there is no detectable difference between the spectra on the two surfaces, as expected. On the other hand, the clearly discernible differences in the spectral intensities for *R*-3MCHO on the Cu(643)$^{R\&S}$ surfaces indicate that the *R*-3MCHO orientation is sensitive to the chirality of their kinks. Reproduced with permission from ref 36. Copyright 2008 American Chemical Society.

selectively adsorbed at the kinks on Cu(643)^S. The mode at 1715 cm^{-1} in the multilayer spectrum is associated with the carbonyl, >C=O, stretch mode. Its red shift in frequency as the coverage decreases is indicative of the interaction of the carbonyl group with the Cu surface. Its decrease in intensity indicates that the molecules go from being randomly orientated in the multilayer to an orientation that has the carbonyl group and its dynamic dipole moment, $\vec{\mu}_{C=O}$, orientated roughly parallel to the Cu(643)^S surface. This understanding is borne out by subsequent DFT modeling of *R*-3MCHO adsorption on the Cu(643)^S surface which shows the carbonyl group interacting with kink in the step edge, as depicted in the inset to Figure 4A.[41] Note that this structure and the corroborating DFT calculations show the highest binding energy site to be the internal kink. The oxygen atom of the ketone is adsorbed to the bridging site between the internal kink Cu atom and the adjacent Cu atom in the (100) step edge.

The enantiospecificity of the *R*-3MCHO orientation when adsorbed at the kinks on the Cu(643)$^{R\&S}$ surfaces is detected by the infrared absorption spectra in Figure 4B. The upper two spectra demonstrate the indistinguishability of the spectra taken for racemic 3MCHO on the Cu(643)$^{R\&S}$ surfaces. This control experiment reveals that structural differences between the two surfaces are limited to their being enantiomorphs. The lower two spectra were obtained from *R*-3MCHO adsorbed at the kinks on the Cu(643)$^{R\&S}$ surfaces. The distinct signal in their difference spectrum is an unequivocal indicator of the fact that *R*-3MCHO must adopt different geometries on the two surface enantiomorphs. As a result, the dynamic dipole moments of *R*-3MCHO's vibrational modes have different projections onto the normal vectors of the Cu(643)$^{R\&S}$ surfaces and, therefore, exhibit different intensities on the two.

https://doi.org/10.1021/accountsmr.1c00145
Acc. Mater. Res. 2021, 2, 1024−1032

5. ENANTIOSPECIFIC ADSORPTION/DESORPTION

5.1. Enantiospecific Desorption Kinetics

Simulations of *trans*-1,2-dimethylcyclopropane enantiomers on $Pt(643)^{R\&S}$ provided the first evidence of enantiospecific adsorption energetics, predicting $\Delta\Delta E_{ads} \cong 4.5$ kJ/mol.[15] Measurements of desorption kinetics using methods such as temperature-programmed desorption (TPD) provided the first experimental estimates of the enantiospecific desorption barriers of chiral adsorbates on chiral surfaces. The first such study of the desorption kinetics of *R*- and *S*-PO on $Cu(643)^{R\&S}$ estimated that $\Delta\Delta E^{\ddagger}_{des} \cong 0.27 \pm 0.06$ kJ/mol.[17] Among the various measurements of enantiospecific desorption energetics on chiral metal surfaces, the highest value observed is $\Delta\Delta E^{\ddagger}_{des} \cong 4$ kJ/mol for the desorption of *R*-methyl lactate from $Cu(643)^{R\&S}$.[42] The largest value that we have observed is $\Delta\Delta E^{\ddagger}_{des} \cong 3$ kJ/mol for D- and L-lysine on $Cu(3,1,17)^{R\&S}$.[43] All of these results point to the fact that diastereomeric enantiomer interaction energetics tend to be weakly enantiospecific; $\Delta\Delta E^{\ddagger}_{des} \cong k_BT$ under most circumstances. This imposes significant challenges to measurement of enantiospecific interaction energetics and even greater challenges to their prediction by simulation.

The most comprehensively studied chiral adsorbate is *R*-3-methylcyclohexanone which has been studied on a set of 21 chiral and achiral $Cu(hkl)^{R\&S}$ surfaces.[41,44−48] *R*-3MCHO has proven to be an inspired/serendipitous choice of chiral probe molecules. As illustrated in Figure 5A, the temperature-programmed desorption spectrum of *R*-3MCHO from chiral $Cu(hkl)^{R\&S}$ surfaces exhibits three peaks (T_p = 230, 345, and 385 K) that have been shown to arise from *R*-3MCHO molecules desorbing from the terrace, step edge, and kink sites, respectively.[45,48] The inset reveals an enantiospecific difference of $\Delta T_p \cong 3.5$ K in the peak desorption temperatures from the chiral kinks on $Cu(643)^{R\&S}$. This translates into an estimated difference in the enantiospecific desorption barriers of $\Delta\Delta E^{\ddagger}_{des} \cong 0.98 \pm 0.18$ kJ/mol. Figure 5B reveals that the magnitude of $\Delta\Delta E^{\ddagger}_{des}$ is ∼1 kJ/mol across a set of seven $Cu(hkl)^{R\&S}$ surfaces with various terrace−step−kink orientations.[48] Figure 5B illustrates another important point; although the surfaces shown are all of *S*-chirality, the sign of $\Delta\Delta E^{\ddagger}_{des}$ can switch across the stereographic triangle.

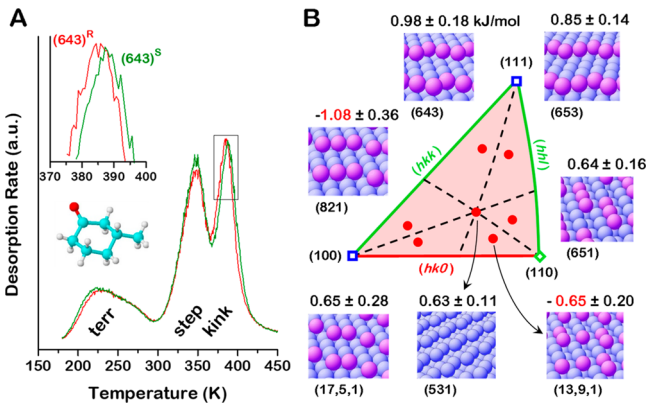

Figure 5. Enantiomer desorption energies are enantiospecific on chiral surfaces. A) The desorption energies of *R*-3MCHO (inset) from $Cu(hkl)^{R\&S}$ surfaces are sensitive to surface chirality. Temperature-programmed desorption spectra of *R*-3MCHO from $Cu(643)^{R\&S}$ reveal three peaks arising from desorption from three sites: 230 K from the (111) terraces, 345 K from the (100) step edges, and 385 K from the (110) kinks. The inset reveals that the desorption temperatures from the chiral kinks differ by ∼3.5 K revealing enantiospecific desorption energetics. B) Stereographic triangle showing the locations and structures of seven chiral $Cu(hkl)^{R\&S}$ surfaces on which enantiospecific *R*-3MCHO desorption energies have been measured. The estimated enantiospecificities of the desorption energies, $\Delta\Delta E^{(hkl)}_{des} = \Delta E^{(hkl)\text{-}S}_{des} - \Delta E^{(hkl)\text{-}R}_{des}$, are shown and all are of order ∼1 kJ/mol. Note, however, that the sign of $\Delta\Delta E^{(hkl)}_{des}$ changes among these surfaces; i.e., the desorption energy of *R*-3MCHO is not always greater on kinks of one chirality than the other. Reproduced with permission from ref 48. Copyright 2017 Institute of Physics.

5.2. Equilibrium Adsorption and Separations

Enantiospecific adsorption energies are the root of adsorption-based enantiomer purification processes. The first evidence of enantiomer purification on an intrinsically chiral metal surface was by a kinetic separation in which a racemic *RS*-3MCHO monolayer was purified during partial desorption from the $Cu(643)^{R\&S}$ surfaces.[45] That experiment did not have or require the ability to discriminate between enantiomers on surfaces but it highlighted the need for surface measurements that can quantify enantiomeric excess in adsorbed enantiomer mixtures. In our hands, this challenge has been solved by using chiral amino acids ($HO_2CCH(NH_2)R$). Because of their importance in biochemistry, the L-amino acids are available in multiple isotopomeric forms, typically labeled with ^{13}C. This enables rigorous determination of surface reaction mechanisms by using mass spectrometry to identify the fate of isotopic labels during amino acid reaction and decomposition.[49,50] More importantly, one can quantify enantiomeric excess on the surface following adsorption of mixtures of unlabeled D- and ^{13}C-labeled L-enantiomers.[51−56]

Enantiomer separation on intrinsically chiral metal surfaces was rigorously demonstrated during equilibrium exposure of $Cu(3,1,17)^{R\&S}$ surfaces (Figure 6A) to mixtures of D-aspartic acid (D-Asp, $HO_2CCH(NH_2)CH_2CO_2H$) and 1,4-$^{13}C_2$-L-Asp ($HO_2{}^{13}CCH(NH_2)CH_2{}^{13}CO_2H$). Figure 6C (blue dots and circles) shows the enantiomeric excess on the surface, ee_s, versus gas phase ee_g.[53] The key result is that in equilibrium with a racemic mixture, $ee_g = 0$, the adsorbed monolayer has $ee_g^R = -ee_g^S \neq 0$. These data reveal an enantiospecific difference in the adsorption free energies of $\Delta\Delta G_{ads} \cong 3$ kJ/mol.

5.3. Enantiomer Separations on *Achiral* Surfaces

During the course of making control measurements of the equilibrium adsorption of D-/L-Asp mixtures onto achiral Cu(111) (Figure 6B) we made the unexpected discovery that $ee_s \neq ee_g$ (Figure 6D, blue dots), except when $ee_g = 0, \pm 1$.[55] In this case, $|ee_s| > |ee_g|$, revealing that even on an achiral surface, enantiopurification can occur during equilibrium adsorption of nonracemic mixtures. This is somewhat surprising, given that there can be no enantiospecific difference in adsorption energies on an achiral surface, $\Delta\Delta E_{ads} = 0$.

Recently, we have conducted Monte Carlo simulations (Figure 6B&D, solid and dashed curves) using the 2D-Ising model to show that the autoamplification of enantiomeric excess can be attributed to nearest neighbor interactions.[57] Specifically, the amplification of enantiomeric excess arises from homochiral (D−D and L−L) interactions that are more attractive than heterochiral (D−L) interactions. Comparison of the data and the Monte Carlo results indicate that the difference in homochiral and heterochiral nearest neighbor interactions is $\Delta\Delta E_{exch}$D−L ≅ 2.5 kJ/mol. One interesting feature to note about this amplification process is that in spite of being driven by a relatively small difference in enantiomer interaction energies, the

https://doi.org/10.1021/accountsmr.1c00145
Acc. Mater. Res. 2021, 2, 1024−1032

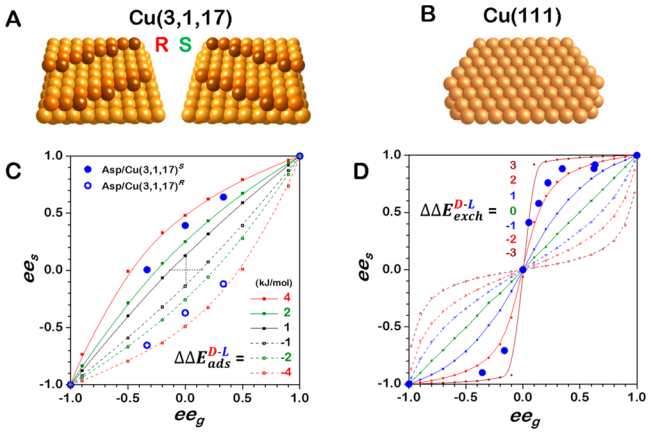

Figure 6. Enantioselective equilibrium adsorption from enantiomer mixtures. A) The ideal structure of the chiral Cu(3,1,17)$^{R\&S}$ surfaces. B) The ideal structure of the achiral Cu(111) surface. C) The surface enantiomeric excess, $ee_s = (\theta_D - \theta_L)/(\theta_D + \theta_L)$), (blue dots and circles) versus gas phase enantiomeric excess, $ee_g = (P_D - P_L)/(P_D + P_L)$), during equilibrium adsorption of D- and L-Asp mixtures onto Cu(3,1,17)$^{R\&S}$ surfaces at 460 K. Note that for a racemic mixture in the gas phase, $ee_g = 0$, the enantiomeric excesses on the surfaces are $ee_s = \pm 0.4$. This demonstrates that equilibrium adsorption onto Cu-(3,1,17)$^{R\&S}$ surfaces leads to enantiomer purification. The solid and dashed curves are fits to a 2D Ising model Monte Carlo simulation of enantiomer adsorption with enantiospecific adsorption energies in the range $\Delta\Delta E_{ads}$D−L = −4 to 4 kJ/mol. D) Plot of ee_s versus ee_g (blue dots) during equilibrium adsorption of D- and L-Asp mixtures onto the achiral Cu(111) surface at 460 K. For the racemic gas phase mixture, $ee_g = 0$, the adsorbed phase is also racemic, $ee_s = 0$, because the Cu(111) surface is achiral. However, when $ee_g \neq 0$, autoamplification leads to $|ee_s| > |ee_g|$. This behavior is predicted by Monte Carlo simulation of the 2D Ising model with $\Delta\Delta E_{exch}$D−L > 0 (solid curves). Reproduced with permission from ref 57. Copyright 2021 Wiley-VCH.

effect is large; an enantiomer ratio of 2:1 in the gas phase, $ee_g = 0.33$, yields an enantiomer ratio of 16:1 on the surface, $ee_s = 0.88$. This is a factor of ∼8 where the Boltzmann factor is ∼2 at the temperature of 460 K. This suggests that some cooperative effects are at work.

6. SUPERENANTIOSPECIFIC EXPLOSION REACTION KINETICS

6.1. Enantiospecificity of First-Order Kinetics

As has been mentioned and demonstrated several times, the enantiospecificities of chiral molecular interactions with chiral environments are small, $O(k_BT)$. In the case of *R*-3MCHO desorption from the chiral kinks on Cu(*hkl*)$^{R\&S}$ surfaces (Figure 5B), the desorption energy difference is $\Delta\Delta E_{des} \cong 1$ kJ/mol and corresponds to a difference in desorption rates of ∼30% at 385 K. The difference in the desorption rates shown in the inset to Figure 5A is clearly small. For a first-order process such as desorption, $r = k\cdot\theta$, where θ is the adsorbate coverage, it would require as yet unachieved $\Delta\Delta E_{des}$ to realize the peak temperature difference needed to significantly increase the enantiospecificity of the desorption rates. However, for highly nonlinear processes such as equilibrium adsorption governed by the Ising model, this is achievable.

6.2. Surface Explosion Reactions

There are a number of adsorbate decomposition reactions with highly nonlinear kinetics analogous to those of radical-mediated gas phase explosions. On surfaces, these are typically vacancy-mediated explosions whereby an adsorbate requires an adjacent empty site in order to decompose. Once the adsorbate decomposes, it leaves two empty sites which beget four, then eight, and so on; the rate of decomposition accelerates autocatalytically until the adsorbate layer is consumed.[3,58,59] It so happens that the decomposition of tartaric acid (TA) and aspartic acid (Asp) on Cu(110) surfaces follow such a mechanism.[49,60,61]

We have demonstrated that on chiral Cu(*hkl*)$^{R\&S}$ surfaces, the highly nonlinear kinetics of surface explosions leads to extremely high enantiospecificity.[62] Figure 7A (solid red and blue curves)

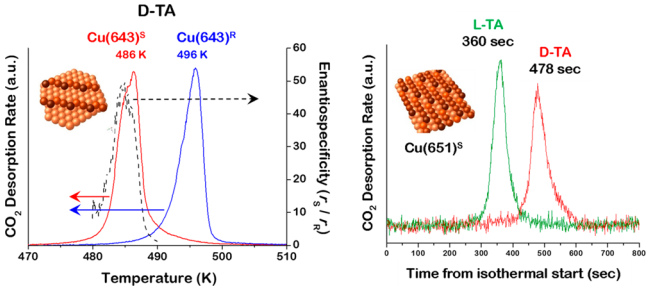

Figure 7. Explosive autocatalytic decomposition of TA enantiomers leads to very high enantioselectivity on chiral surfaces. A) TPR spectra of D-TA decomposition to CO_2 on the Cu(643)$^{R\&S}$ surfaces at initial coverages of $\theta_{TA} = 1$ ML. Because of the explosion mechanism, the peaks are very narrow and well-resolved. The ratio of reaction rates (dashed black curve) reaches rD-TA$^{(643)\text{-}S}$/rD-TA$^{(643)\text{-}R} \cong 50$. B) Isothermal TPR spectra of L- and D-TA decomposition into CO_2 at 450 K on Cu(651)^S. The vacancy-mediated explosion mechanism leads to long initiation periods followed by explosive autocatalytic acceleration of the rates. The ratio of the reaction rates at 360 s is rL-TA$^{(651)\text{-}S}$/rD-TA$^{(651)\text{-}S} \cong 15$. Reproduced with permission from ref 62. Copyright 2013 American Chemical Society.

illustrates temperature-programmed reaction spectra obtained for D-TA decomposition on Cu(643)$^{R\&S}$ surfaces.[62] The peaks for CO_2 desorption from TA decomposition are quite narrow and well resolved. This is a direct consequence of the nonlinear rate law for vacancy-mediated surface explosion kinetics.[59] The key point is that comparison of the rates (Figure 7A, dashed black curve) on the Cu(*hkl*)$^{R\&S}$ surfaces at $T = 486$ K reveals an enantiospecificity of rD-TA^S/rD-TA$^R \cong 50$![62] The data in Figure 7B illustrate another manifestation of the same phenomenon in which we have measured the rates of D- and L-TA decomposition on Cu(651)^S versus time at 450 K. In this case, the enantiospecificity of the decomposition rates at $t = 400$ s is rL-TA^S/rD-TA$^S \cong 15$. Both the explosion reactions and the autoamplification of enantiomeric excess during equilibrium adsorption (Figure 6D) are examples of processes for circumventing inherently low enantiospecific interaction energetics to achieve high enantiospecificity.

7. STRUCTURE SENSITIVITY ON CHIRAL SURFACES

The demonstration that surface reactions and catalytic surface chemistry are dictated by surface structure and crystallographic orientation is one of the great achievements of modern surface science.[63] Enantioselectivity is the quintessential form of structure sensitivity. The two enantiomers of a chiral surface have identical physical properties and identical interactions with achiral adsorbates. What yields enantiospecific interactions with chiral adsorbates is the dissymmetry of the surface structure. This begs the question, Which surface orientation leads to the

https://doi.org/10.1021/accountsmr.1c00145
Acc. Mater. Res. 2021, 2, 1024−1032

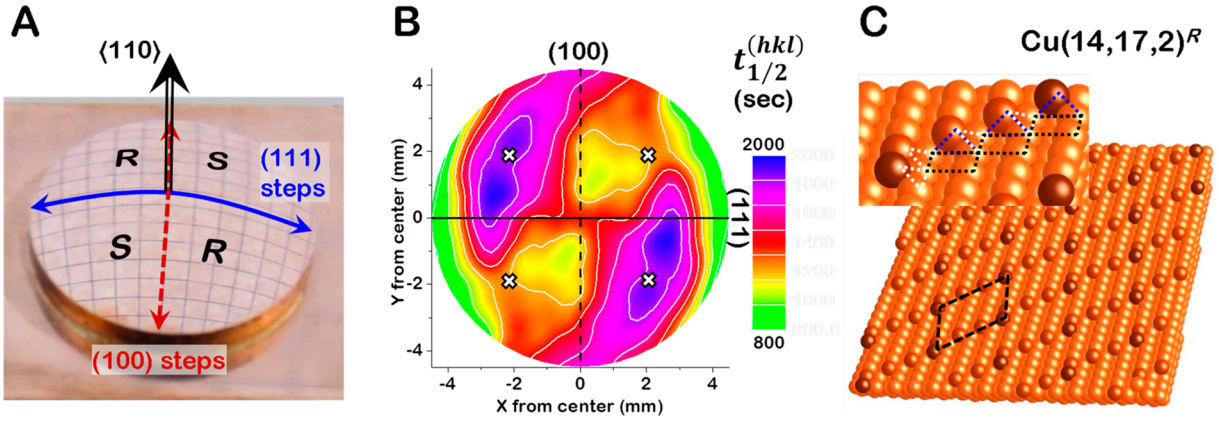

Figure 8. High throughput mapping of surface structure dependent enantiospecificity. A) A curved Cu(110) surface structure spread single crystal (S^4C) exposes the Cu(110) plane at the center and all surface orientations within 14° of the [110] direction. The 2-fold symmetry yields four quadrants around the (110) point having alternating *R*- and *S*-chirality. (B) Map of $t_{1/2}^{(hkl)}$ for D-TA decomposition measured at 169 points distributed across the Cu(110)-S^4C. Comparison of the values of $t_{1/2}^{(hkl)}$ between enantiomorphous surface orientations identifies the surface orientation with the greatest enantiospecificity, i.e., the maximum value of $\Delta t_{1/2}^{(hkl)} = t_{1/2}^{(hkl)\text{-}R} - t_{1/2}^{(hkl)\text{-}S}$. That occurs at the four points marked with ×. D) The structure of Cu(14,17,2), the most enantiospecific surface for TA decomposition lying in the vicinity of Cu(110). Reproduced with permission from ref 64. Copyright 2019 American Chemical Society.

highest enantiospecificity for a given adsorbate or reaction? Perhaps a more challenging proposition is, how do you design a surface structure that yields the highest enantiospecificity? Figure 5B summarizes our earliest attempt to begin addressing this problem by measuring the enantiospecific desorption kinetics of *R*-3-methylcyclohexanone on seven chiral Cu(*hkl*)$^{R\&S}$ surfaces spanning the stereographic projection.[45−48] These data revealed the fact that $\Delta\Delta E_{des}^{R-S}$ varies measurably and that it can change sign, but that its range is small, $\Delta\Delta E_{des}^{R-S}$ = 1 to −1 kJ/mol. Note, that study involved the use of 23 different single crystal surfaces (9 achiral plus 2 × 7 chiral orientations) and took several years of effort.

7.1. High Throughput Sampling of Surface Structure Space

In order to measure structure sensitive rate constants that span surface orientation space comprehensively, we have coupled the highly enantiospecific tartaric acid surface explosion reaction with a high throughput methodology for rapidly sampling surface orientation space. Figure 8A is a photograph of a surface structure spread single crystal (S^4C), in this case, a Cu(110) crystal that has been shaped into a spherical dome with the Cu(110) surface at the center. The dome has a radius of curvature of 21 mm exposing all surfaces within 14° of the [110] direction, all on one sample. Note that the Cu(110) surface has 2-fold rotational symmetry meaning that it exposes two quadrants that expose identical sets of surface with *S*-orientations and two quadrants exposing *R*-orientations.

The experiment that maps enantiospecificity across the S^4C surfaces begins by adsorption of a saturated monolayer of D-TA such that $\theta_{TA}^{(hkl)}(t = 0) = 1$. X-ray photoemission spectroscopy is used to measure surface composition at 169 different points cross the S^4C surface, thereby creating maps of local surface compositions. With the surface heated at 433 K, the local coverage on 169 surface orientations is measured periodically to obtain $\theta_{TA}^{(hkl)}(t)$ as the D-TA decomposes. The simplest kinetic parameter extracted from the data is $t_{1/2}^{(hkl)}$, the time at which the local coverage drops to half its initial value (Figure 8B).[64] This clearly reveals the surface structure sensitivity of D-TA decomposition on all surfaces vicinal to Cu(110). From this map, one can identify the surface orientation (×) exhibiting the greatest value of $\Delta t_{1/2} = t_{1/2}^{(hkl)\text{-}R} - t_{1/2}^{(hkl)\text{-}S}$, i.e., the greatest enantiospecificity.

7.2. Most Enantioselective Surfaces: Cu(14,17,2)

Among surface orientations vicinal to Cu(110), the Cu(14,17,2) surface shown in Figure 8C exhibits the greatest enantiospecificity toward TA decomposition. The ideal structure of this surface is based on (110) terraces with kinked steps running at ∼45° with respect to the (110) rows. Close inspection of the step edge reveals two types of kink atoms. The underlying reason why this structure should yield a maximum in enantiospecificity for TA decomposition remains an open and challenging question. In thinking about this problem, it will be important to bear in mind that the adsorption of TA might induce a change in surface structure that is key to understanding the origin of its enantioselectivity. Nonetheless, the demonstrated ability to identify this surface as "special" is a significant step toward understanding surface structure sensitive enantioselectivity.

8. CONCLUSIONS AND PERSPECTIVE

Twenty five years ago, when it was first realized that high Miller index metals surface are chiral, there was nothing known about their enantiospecific surface chemistry. Herein, we have documented the progressive evolution of our understanding of chiral surface structure, enantiospecific adsorption, and enantiospecific surface chemistry. Like most enantiospecific chemistry, the fundamental energetics leading to enantioselectivity on surfaces are small, $O(k_BT)$. Nonetheless, this can be circumvented by nonlinear processes that effectively amplify these small energetic differences.[3]

Challenges for the future include the further engagement of molecular simulation to provide levels of insight that cannot be achieved solely by experiment. The key difficulty here is the fact that the small enantiospecificities of the relevant energetics are on the edge of current computational accuracy. Equally important for the ultimate application of intrinsically chiral metal surfaces is the need to develop methods for their scalable preparation with surface areas that have practical utility. A recent perspective article provides some thoughts on this issue and suggests several possible routes to the scalable manufacturing of intrinsically chiral metal surfaces.[65] This may be achievable using

https://doi.org/10.1021/accountsmr.1c00145
Acc. Mater. Res. 2021, 2, 1024−1032

nanoparticle synthesis methods, chiral imprinting of metals, or other creative and as yet unimagined methods.

AUTHOR INFORMATION

Corresponding Author

Andrew J. Gellman − *Department of Chemical Engineering and W. E. Scott Institute for Energy Innovation, Carnegie Mellon University, Pittsburgh, Pennsylvania 15213, United States;* orcid.org/0000-0001-6618-7427; Phone: 1-412-268-3848; Email: gellman@cmu.edu

Complete contact information is available at: https://pubs.acs.org/10.1021/accountsmr.1c00145

Notes

The author declares no competing financial interest.

Biography

Andrew Gellman received a BS in chemistry in 1981 from the California Institute of Technology and a PhD in Physical Chemistry in 1985 from the University of California Berkeley. He then held an ICI Postdoctoral Fellowship at the University of Cambridge before starting his independent research career at the University of Illinois Urbana−Champaign in 1986. In 1992, he moved to Carnegie Mellon University where he is currently the Lord Chair in Chemical Engineering. From 2003 to 2013 he served as Department Head of Chemical Engineering. In addition to his long-standing interest in the enantioselective surface chemistry of chiral metal surfaces, Professor Gellman has worked in the fields of tribological surface chemistry and catalytic surface chemistry. Over the past decade, he has devoted significant effort to the development of tools for the study of alloys using high throughput methods that can span entire binary and ternary alloy composition spaces. Similarly, he has developed the use of spherically shaped metal single crystals for comprehensive studies of structure sensitive surface chemistry across continuous regions of surface orientation space.

ACKNOWLEDGMENTS

Components of this work have been support over the years by funding from both the US National Science Foundation and the US Department of Energy. Current funding is acknowledged under grant number NSF CHE1764252. The work summarized in this Account would not have been possible without the efforts and insights of a large number of students and collaborators.

REFERENCES

(1) McFadden, C. F.; Cremer, P. S.; Gellman, A. J. Adsorption of chiral alcohols on ''chiral'' metal surfaces. *Langmuir* **1996**, *12* (10), 2483−2487.
(2) Jenkins, S. R. *Chirality at Solid Surfaces*, 1st ed.; John Wiley & Sons: Hoboken, NJ, 2018; p 355.
(3) Gellman, A. J.; Ernst, K. H. Chiral Autocatalysis and Mirror Symmetry Breaking. *Catal. Lett.* **2018**, *148* (6), 1610−1621.
(4) Bonner, W. A. The origin and amplification of biomolecular chirality. *Origins Life Evol. Biospheres* **1991**, *21* (2), 59−111.
(5) Bada, J. L. Origins of homochirality. *Nature* **1995**, *374*, 594.
(6) Klussmann, M.; Blackmond, D. G. Origin of Homochirality. *ACS Symp. Ser.* **2010**, *1025*, 133−145.
(7) Nguyen, L. A.; He, H.; Pham-Huy, C. Chiral drugs: an overview. *Int. J. Biomed. Sci.: IJBS* **2006**, *2* (2), 85−100.
(8) Kelso, M. V.; Tubbesing, J. Z.; Chen, Q. Z.; Switzer, J. A. Epitaxial Electrodeposition of Chiral Metal Surfaces on Silicon(643). *J. Am. Chem. Soc.* **2018**, *140* (46), 15812−15819.
(9) Sholl, D. S.; Asthagiri, A.; Power, T. D. Naturally chiral metal surfaces as enantiospecific adsorbents. *J. Phys. Chem. B* **2001**, *105* (21), 4771−4782.
(10) Prinz, J.; Groning, O.; Brune, H.; Widmer, R. Highly Enantioselective Adsorption of Small Prochiral Molecules on a Chiral Intermetallic Compound. *Angew. Chem., Int. Ed.* **2015**, *54* (13), 3902−3906.
(11) Stolz, S.; Yakutovich, A. V.; Prinz, J.; Dienel, T.; Pignedoli, C. A.; Brune, H.; Groning, O.; Widmer, R. Near-Enantiopure Trimerization of 9-Ethynylphenanthrene on a Chiral Metal Surface. *Angew. Chem., Int. Ed.* **2020**, *59* (41), 18179−18183.
(12) Ben-Moshe, A.; Govorov, A. O.; Markovich, G. Enantioselective Synthesis of Intrinsically Chiral Mercury Sulfide Nanocrystals. *Angew. Chem., Int. Ed.* **2013**, *52* (4), 1275−1279.
(13) Ben-Moshe, A.; Wolf, S. G.; Bar Sadan, M.; Houben, L.; Fan, Z. Y.; Govorov, A. O.; Markovich, G. Enantioselective control of lattice and shape chirality in inorganic nanostructures using chiral biomolecules. *Nat. Commun.* **2014**, *5*, 4302.
(14) Gellman, A. J.; Horvath, J. D.; Buelow, M. T. Chiral single crystal surface chemistry. *J. Mol. Catal. A: Chem.* **2001**, *167* (1−2), 3−11.
(15) Sholl, D. S. Adsorption of chiral hydrocarbons on chiral platinum surfaces. *Langmuir* **1998**, *14* (4), 862−867.
(16) Ahmadi, A.; Attard, G.; Feliu, J.; Rodes, A. Surface reactivity at "chiral" platinum surfaces. *Langmuir* **1999**, *15* (7), 2420−2424.
(17) Horvath, J. D.; Gellman, A. J. Enantiospecific desorption of R- and S-propylene oxide from a chiral Cu(643) surface. *J. Am. Chem. Soc.* **2001**, *123* (32), 7953−7954.
(18) van Hove, M. A.; Somorjai, G. A. New Microfacet Notation for High-Miller-Index Surfaces of Cubic Materials with Terrace, Step and Kink Structures. *Surf. Sci.* **1980**, *92* (2−3), 489−518.
(19) Attard, G. A.; Ahmadi, A.; Feliu, J.; Rodes, A.; Herrero, E.; Blais, S.; Jerkiewicz, G. Temperature effects in the enantiomeric electro-oxidation of D- and L-glucose on Pt{643}(S). *J. Phys. Chem. B* **1999**, *103* (9), 1381−1385.
(20) Jenkins, S. J.; Pratt, S. J. Beyond the surface atlas: A roadmap and gazetteer for surface symmetry and structure. *Surf. Sci. Rep.* **2007**, *62* (10), 373−429.
(21) Einstein, T. L.; Jung, T. M.; Bartelt, N. C.; Williams, E. D.; Rottman, C. Step doubling and related transitions on vicinal surfaces. *J. Vac. Sci. Technol., A* **1992**, *10* (4), 2600−2605.
(22) Jeong, H. C.; Williams, E. D. Steps on surfaces: experiment and theory. *Surf. Sci. Rep.* **1999**, *34* (6−8), 171−294.
(23) Schilling, A. C.; Therrien, A. J.; Hannagan, R. T.; Marcinkowski, M. D.; Kress, P. L.; Patel, D. A.; Balema, T. A.; Larson, A. M.; Lucci, F. R.; Coughlin, B. P.; Zhang, R. Q.; Thuening, T.; Cinar, V.; McEwen, J. S.; Gellman, A. J.; Sykes, E. C. H. Templated Growth of a Homochiral Thin Film Oxide. *ACS Nano* **2020**, *14* (4), 4682−4688.
(24) de Alwis, A.; Holsclaw, B.; Pushkarev, V. V.; Reinicker, A.; Lawton, T. J.; Blecher, M. E.; Sykes, E. C. H.; Gellman, A. J. Surface Structure Spread Single Crystals (S^4Cs): Preparation and characterization. *Surf. Sci.* **2013**, *608*, 80−87.
(25) Baber, A. E.; Gellman, A. J.; Sholl, D. S.; Sykes, E. C. H. The real structure of naturally chiral Cu{643}. *J. Phys. Chem. C* **2008**, *112* (30), 11086−11089.
(26) Power, T. D.; Asthagiri, A.; Sholl, D. S. Atomically detailed models of the effect of thermal roughening on the enantiospecificity of naturally chiral platinum surfaces. *Langmuir* **2002**, *18* (9), 3737−3748.
(27) Puisto, S. R.; Held, G.; Ranea, V.; Jenkins, S. J.; Mola, E. E.; King, A. A. The structure of the chiral Pt{531} surface: A combined LEED and DFT study. *J. Phys. Chem. B* **2005**, *109* (47), 22456−22462.
(28) Dutta, S.; Gellman, A. J. Enantiomer surface chemistry: conglomerate versus racemate formation on surfaces. *Chem. Soc. Rev.* **2017**, *46* (24), 7787−7839.
(29) Ernst, K. H. Molecular chirality at surfaces. *Phys. Status Solidi B* **2012**, *249* (11), 2057−2088.
(30) Barlow, S. M.; Raval, R. Complex organic molecules at metal surfaces: bonding, organisation and chirality. *Surf. Sci. Rep.* **2003**, *50* (6−8), 201−341.

(31) Raval, R. Chiral expression from molecular assemblies at metal surfaces: insights from surface science techniques. *Chem. Soc. Rev.* **2009**, *38* (3), 707−721.
(32) Mark, A. G.; Forster, M.; Raval, R. Recognition and Ordering at Surfaces: The Importance of Handedness and Footedness. *ChemPhysChem* **2011**, *12* (8), 1474−1480.
(33) Greber, T.; Sljivancanin, Z.; Schillinger, R.; Wider, J.; Hammer, B. Chiral recognition of organic molecules by atomic kinks on surfaces. *Phys. Rev. Lett.* **2006**, *96* (5), 056103.
(34) Schillinger, R.; Sljivancanin, Z.; Hammer, B.; Greber, T. Probing enantioselectivity with x-ray photoelectron spectroscopy and density functional theory. *Phys. Rev. Lett.* **2007**, *98* (13), 136102.
(35) Gladys, M. J.; Stevens, A. V.; Scott, N. R.; Jones, G.; Batchelor, D.; Held, G. Enantiospecific adsorption of alanine on the chiral Cu{531} surface. *J. Phys. Chem. C* **2007**, *111* (23), 8331−8336.
(36) Horvath, J. D.; Baker, L.; Gellman, A. J. Enantiospecific orientation of R-3-Methylcyclohexanone on the chiral Cu(643)(R/S) surfaces. *J. Phys. Chem. C* **2008**, *112* (20), 7637−7643.
(37) Thomsen, L.; Tadich, A.; Riley, D. P.; Cowie, B. C. C.; Gladys, M. J. Investigating the Enantioselectivity of Alanine on a Chiral Cu{421}(R) Surface. *J. Phys. Chem. C* **2012**, *116* (17), 9472−9480.
(38) Clegg, M. L.; de la Garza, L. M.; Karakatsani, S.; King, D. A.; Driver, S. M. Chirality in Amino Acid Overlayers on Cu Surfaces. *Top. Catal.* **2011**, *54* (19−20), 1429−1444.
(39) Street, S. C.; Gellman, A. J. Quantitative adsorbate orientation from vibrational spectra: Ethoxides on Cu(111). *J. Chem. Phys.* **1996**, *105* (16), 7158−7170.
(40) Street, S. C.; Gellman, A. J. FT-IRAS of adsorbed alkoxides: Fluorinated ethoxides on Cu(111). *J. Phys. Chem.* **1996**, *100* (20), 8338−8348.
(41) Wei, D. S.; Mhatre, B. S.; Gellman, A. J.; Sholl, D. S. Contributions of dispersion forces to R-3-methylcyclohexanone physisorption on low and high Miller index Cu surfaces. *Surf. Sci.* **2014**, *629*, 35−40.
(42) Fleming, C.; King, M.; Kadodwala, M. Highly Efficient Electron Beam Induced Enantioselective Surface Chemistry. *J. Phys. Chem. C* **2008**, *112* (47), 18299−18302.
(43) Cheong, W. Y.; Gellman, A. J. Energetics of Chiral Imprinting of Cu(100) by Lysine. *J. Phys. Chem. C* **2011**, *115* (4), 1031−1035.
(44) Horvath, J. D.; Gellman, A. J. Enantiospecific desorption of chiral compounds from chiral Cu(643) and achiral Cu(111) surfaces. *J. Am. Chem. Soc.* **2002**, *124* (10), 2384−2392.
(45) Horvath, J. D.; Koritnik, A.; Kamakoti, P.; Sholl, D. S.; Gellman, A. J. Enantioselective separation on a naturally chiral surface. *J. Am. Chem. Soc.* **2004**, *126* (45), 14988−14994.
(46) Huang, Y.; Gellman, A. J. Enantiospecific adsorption of (R)-3-Methylcyclohexanone on naturally chiral Cu(531)(R&S) surfaces. *Catal. Lett.* **2008**, *125* (3−4), 177−182.
(47) Huang, Y.; Gellman, A. J. Enantiospecific Adsorption of (R)-3-Methylcyclohexanone on Naturally Chiral Surfaces Vicinal to Cu(110). *Top. Catal.* **2011**, *54* (19−20), 1403−1413.
(48) Gellman, A. J.; Huang, Y.; Koritnik, A. J.; Horvath, J. D. Structure-sensitive enantiospecific adsorption on naturally chiral Cu(hkl)(R&S) surfaces. *J. Phys.: Condens. Matter* **2017**, *29* (3), 034001.
(49) Mhatre, B. S.; Dutta, S.; Reinicker, A.; Karagoz, B.; Gellman, A. J. Explosive enantiospecific decomposition of aspartic acid on Cu surfaces. *Chem. Commun.* **2016**, *52* (98), 14125−14128.
(50) Karagoz, B.; Reinicker, A.; Gellman, A. J. Kinetics and mechanism of aspartic acid adsorption and its explosive decomposition on Cu(100). *Langmuir* **2019**, *35*, 2925−2933.
(51) Dutta, S.; Gellman, A. J. Enantiospecific Adsorption and Decomposition of D- and L-Asp Mixtures on Cu(643)(R&S). *Chimia* **2018**, *72* (6), 404−410.
(52) Dutta, S.; Gellman, A. J. Enantiospecific equilibrium adsorption and chemistry of d-/l-proline mixtures on chiral and achiral Cu surfaces. *Chirality* **2020**, *32* (2), 200−214.
(53) Yun, Y. J.; Gellman, A. J. Enantioselective Separation on Naturally Chiral Metal Surfaces: d, l-Aspartic Acid on Cu(3,1,17)-(R&S) Surfaces. *Angew. Chem., Int. Ed.* **2013**, *52* (12), 3394−3397.
(54) Yun, Y. J.; Wei, D.; Sholl, D. S.; Gellman, A. J. Equilibrium Adsorption of D- and L-Alanine Mixtures on Naturally Chiral Cu{3,1,17}(R&S) Surfaces. *J. Phys. Chem. C* **2014**, *118* (27), 14957−14966.
(55) Yun, Y. J.; Gellman, A. J. Adsorption-induced auto-amplification of enantiomeric excess on an achiral surface. *Nat. Chem.* **2015**, *7* (6), 520−525.
(56) Yun, Y. J.; Gellman, A. J. Enantiospecific Adsorption of Amino Acids on Naturally Chiral Cu{3,1,17}(R&S) Surfaces. *Langmuir* **2015**, *31* (22), 6055−6063.
(57) Dutta, S.; Yun, Y. J.; Widom, M.; Gellman, A. J. 2D Ising Model for Adsorption-induced Enantiopurification of Racemates. *ChemPhysChem* **2021**, *22* (2), 197−203.
(58) Falconer, J. L.; McCarty, J. G.; Madix, R. J. Surface Explosion - HCOOH on Ni (110). *Surf. Sci.* **1974**, *42* (1), 329−330.
(59) Mhatre, B. S.; Pushkarev, V.; Holsclaw, B.; Lawton, T. J.; Sykes, E. C. H.; Gellman, A. J. A Window on Surface Explosions: Tartaric Acid on Cu(110). *J. Phys. Chem. C* **2013**, *117* (15), 7577−7588.
(60) Lorenzo, M. O.; Humblot, V.; Murray, P.; Baddeley, C. J.; Haq, S.; Raval, R. Chemical transformations, molecular transport, and kinetic barriers in creating the chiral phase of (R, R)-tartaric acid on Cu(110). *J. Catal.* **2002**, *205* (1), 123−134.
(61) Behzadi, B.; Romer, S.; Fasel, R.; Ernst, K. H. Chiral recognition in surface explosion. *J. Am. Chem. Soc.* **2004**, *126* (30), 9176−9177.
(62) Gellman, A. J.; Huang, Y.; Feng, X.; Pushkarev, V. V.; Holsclaw, B.; Mhatre, B. S. Superenantioselective Chiral Surface Explosions. *J. Am. Chem. Soc.* **2013**, *135* (51), 19208−19214.
(63) Ertl, G. Reactions at surfaces: From atoms to complexity (Nobel lecture). *Angew. Chem., Int. Ed.* **2008**, *47* (19), 3524−3535.
(64) Karagoz, B.; Payne, M. A.; Reinicker, A.; Kondratyuk, P.; Gellman, A. J. A Most Enantioselective Chiral Surface: Tartaric Acid on All Surfaces Vicinal to Cu(110). *Langmuir* **2019**, *35*, 16438.
(65) Shukla, N.; Gellman, A. J. Chiral metal surfaces for enantioselective processes. *Nat. Mater.* **2020**, *19* (9), 939−945.

https://doi.org/10.1021/accountsmr.1c00145
Acc. Mater. Res. 2021, 2, 1024−1032